RESEARCH PAPER

Formation of modulated structures in single-crystalline hexagonal α-Fe$_2$O$_3$ nanowires

R. S. Cai · T. Li · Y. Q. Wang · C. Wang · L. Yuan · G. W. Zhou

Abstract The microstructures and growth mechanism of Fe$_2$O$_3$ nanowires (NWs) synthesized by thermal oxidation of iron are studied in detail by transmission electron microscopy. Three different structures, single-crystalline, bicrystalline, and tricrystalline, are observed in the NWs. It is found that single-crystalline Fe$_2$O$_3$ NWs have a hexagonal structure while bicrystalline and tricrystalline NWs possess a cubic one. The differences in the electronic structures of the three Fe$_2$O$_3$ NWs are examined by electron energy-loss spectroscopy. A modulated structure with a periodicity of 1.53 nm is observed in single-crystalline Fe$_2$O$_3$ NWs, but not in bicrystalline or tricrystalline Fe$_2$O$_3$ NWs. The formation of the modulated structure in single-crystalline NWs is attributed to the periodical appearance of stacking faults, because of the shear stress occurred during the growth process. NWs possessing a cubic γ-Fe$_2$O$_3$ structure tend to coalesce into the bicrystalline or tricrystalline NWs whereas NWs with the hexagonal α-Fe$_2$O$_3$ structure prefer to grow as single-crystalline NWs. The formation mechanism of Fe$_2$O$_3$ NWs with the different morphologies is discussed.

Keywords Fe$_2$O$_3$ nanowires · Modulated structure · HRTEM · EELS

R. S. Cai · T. Li · Y. Q. Wang (✉) · C. Wang
The Cultivation Base for State Key Laboratory,
Qingdao University, No. 308 Ningxia Road,
Qingdao 266071, People's Republic of China
e-mail: yqwang@qdu.edu.cn

L. Yuan · G. W. Zhou
Department of Mechanical Engineering &
Multidisciplinary Program in Materials Science
and Engineering, State University of New York,
Binghamton, NY 13902, USA

Introduction

Fe$_2$O$_3$ is the most stable iron oxide under the ambient conditions. Because of its high resistivity to corrosion, low toxicity (Cornell and Schwertmann 2003), and great potential for a wide range of applications in the field of catalysts (Liu and Huang 2005), gas sensors, electrode materials (Chen et al. 2005), magnetic recording media (Tepper et al. 2003), and spintronic devices (Shimojo et al. 2006; Zhang et al. 2004), significant effort has been focused on the synthesis of nanostructured Fe$_2$O$_3$. Recently, Fe$_2$O$_3$ nanowires (NWs) have been successfully synthesized by the thermal oxidation of iron in an oxygen-containing atmosphere (Chen et al. 2008b; Chueh et al. 2006; Cvelbar et al. 2008; Dong et al. 2010; Fu et al. 2001; Han et al. 2007; Hiralal et al. 2008; Nasibulin et al. 2009; Rachauskas et al. 2009; Srivastava et al. 2007; Wang et al. 2005a; Wen et al. 2005). Thermal oxidation has received considerable attention because of its technical simplicity and large-scale synthesis of

high-quality Fe_2O_3 NWs (Chen et al. 2008b; Chueh et al. 2006; Cvelbar et al. 2008; Dong et al. 2010; Fu et al. 2001; Han et al. 2007; Hiralal et al. 2008; Nasibulin et al. 2009; Rachauskas et al. 2009; Srivastava et al. 2007; Wang et al. 2005a; Wen et al. 2005). Extensive study has been carried out to understand the growth mechanism of Fe_2O_3 NWs from the oxidation. Some study suggested that the growth of the oxide NWs occurred as a result of the accumulation and relaxation of compressive stresses during the oxidation process (Chen et al. 2008a; Goncalves et al. 2009; Kumar et al. 2004; Mema et al. 2011; Yuan et al. 2011). However, the microscopic processes leading to the oxide NW formation is still unclear because of the lack of the growth details of these one-dimensional oxide structures. A detailed study on the microstructure of Fe_2O_3 NWs is highly desired since it will provide significant insight into understanding the growth mechanism.

In this article, we report on the microstructural investigation of Fe_2O_3 NWs synthesized by thermal oxidation using scanning electron microscopy (SEM) and high-resolution transmission electron microscopy (HRTEM). Three different kinds of morphologies have been observed, namely, single-crystalline, bicrystalline, and tricrystalline NWs, which possess two different crystal structures. In addition, different electronic structures are observed in the NWs with the different structures by electron energy-loss spectroscopy (EELS). A modulated structure is observed only in the single-crystalline NWs, but not in the bicrystalline and tricrystalline NWs. Although modulated structures in Fe_2O_3 NWs were observed previously (Nasibulin et al. 2009), the formation mechanism of such a modulated structure has not been clarified yet. Herein, a mechanism based on our HRTEM observations is proposed to account for the formation of the modulated structure in single-crystalline NWs. Modulated structures are known to play an important role in the synthesis, stabilization as well as the properties in many structures such as ZnS (Jiang et al. 2003), InAs/InP (Bjork et al. 2002), GaP/GaAs, and n-Si/p-Si (Gudiksen et al. 2002) NWs. The elucidation of the mechanism governing the formation of the modulated structure in single-crystalline Fe_2O_3 NWs is a prerequisite for controlling the microstructure of the NWs and correspondingly their properties for practical applications.

Experimental details

The Fe_2O_3 NWs were synthesized by thermal oxidation of iron foil. First, the high-purity (99.99 %) iron foils were thoroughly rinsed with deionized water followed by ultrasonication in acetone for 5 min. Then, the cleaned iron substrates were put on a substrate heater in the vacuum chamber, and the temperature was monitored using a K-type thermocouple in contact with the heater. The chamber was pumped to a vacuum of about 2×10^{-6} Torr, and then filled with 200 Torr oxygen (oxygen purity: 99.999 %). Subsequently, the chamber was sealed, and the iron foil was heated to 600 °C at a rate of 20 °C/min in the oxygen gas. After the iron foil was oxidized for 1 h, it was then cooled down in the same oxygen atmosphere to room temperature at a rate of $\sim$10 °C/min. Morphology and chemical composition of the oxidized samples were investigated using a field emission gun-scanning electron microscope (FEG-SEM) FEI Supra 55VP. Cross-sectional specimens of the oxidized iron foil for transmission electron microscopy (TEM) observations were prepared using conventional techniques of mechanical polishing and ion-thinning. The ion-thinning was carried out using Gatan model 691 precision ion polishing system (PIPS). TEM samples of Fe_2O_3 NWs were prepared by peeling off the black products from the surface of the oxidized iron foil, then ultrasonicating them in ethanol for several minutes, and dispersing a drop onto a holey-carbon-film-coated copper grid. Selected-area electron diffraction (SAED), bright field (BF), and HRTEM were carried out using a JEOL 2100F TEM operated at 200 kV. EELS was performed on an FEI Tecnai F20 TEM. All the EELS spectra were acquired in the image mode with a collection half angle of $\sim$16 mrad.

Results and discussion

Figure 1a shows a typical cross-sectional SEM image of oxidized iron foil. It can be seen that there are four different layers from the iron substrate to its surface, which can be identified as FeO, Fe_3O_4, Fe_2O_3, and Fe_2O_3 NWs by X-ray energy dispersive spectroscopy (EDS) analysis (Yuan et al. 2012). Although the EDS measurements of the compositions do not match exactly with the atomic ratios of the Fe and O for

the different oxide phases, the results are in the reasonable range of the stoichiometry for the different oxide phases. In addition, similar layered structures have also been reported in the literature (Nasibulin et al. 2009). The thicknesses of the three oxide layers are about 4.6, 2.5, and 0.6 μm, respectively. In addition, FeO and Fe_3O_4 layers are composed of coarse grains whereas the outer Fe_2O_3 layer consists of considerably fine grains. Dense Fe_2O_3 NWs ranging from 1.9 to 2.5 μm in length are covered on the surface of the oxidized iron foil. These oxide NWs show a tapered shape at the top, and are relatively aligned and perpendicular to the substrate surface.

Fe$_2$O$_3$ has three different structures α-Fe_2O_3, γ-Fe_2O_3, and ε-Fe_2O_3. To clarify the crystal structures of Fe_2O_3 layer and Fe_2O_3 NWs, and determine the epitaxial relationship between Fe_2O_3 NWs and their root regions, the cross-sectional sample has been extensively examined by TEM. Closer view from the

surface of the Fe_2O_3 layer is shown in Fig. 1b. The insets in Fig. 1b are SAED patterns taken from the NWs and corresponding root regions, respectively. It can be seen that the Fe_2O_3 NWs are formed on top of the grains in the Fe_2O_3 layer and are almost perpendicular to its surface, consistent with our SEM observations. Through the indexing of the SAED patterns, two different structures are confirmed: hexagonal α-Fe_2O_3 and cubic γ-Fe_2O_3. The SAED pattern of the left NW in Fig. 1b can be indexed using the lattice parameters of hexagonal α-Fe_2O_3 ($a = 5.034$ Å, $c = 13.75$ Å), while the SAED pattern of the right one can be indexed using the lattice parameters of cubic γ-Fe_2O_3 ($a = 8.34$ Å). In addition, the root regions have the same structures with the corresponding NWs, as shown in the insets of Fig. 1b. Careful examination of the SAED pattern for the left NW shows that there are many superlattice spots in the SAED pattern, suggesting that the NW has

Fig. 1 a Cross-sectional SEM image of Fe substrate oxidized at 600 °C for 1 h; b cross-sectional BF TEM image showing the NW and the NW root region with the same structures. The *insets* are SAED patterns taken from the NWs and their root regions, respectively; c BF TEM image of cross-sectional sample with grain A tilted to a zone-axis, showing clear grain boundaries
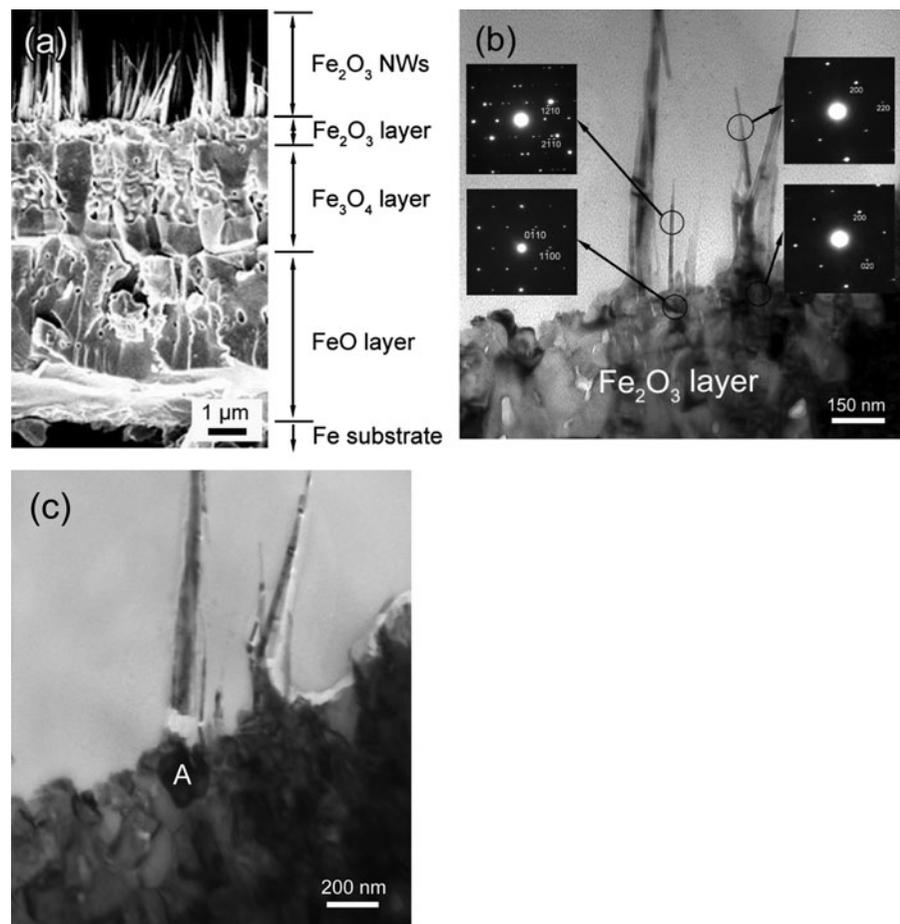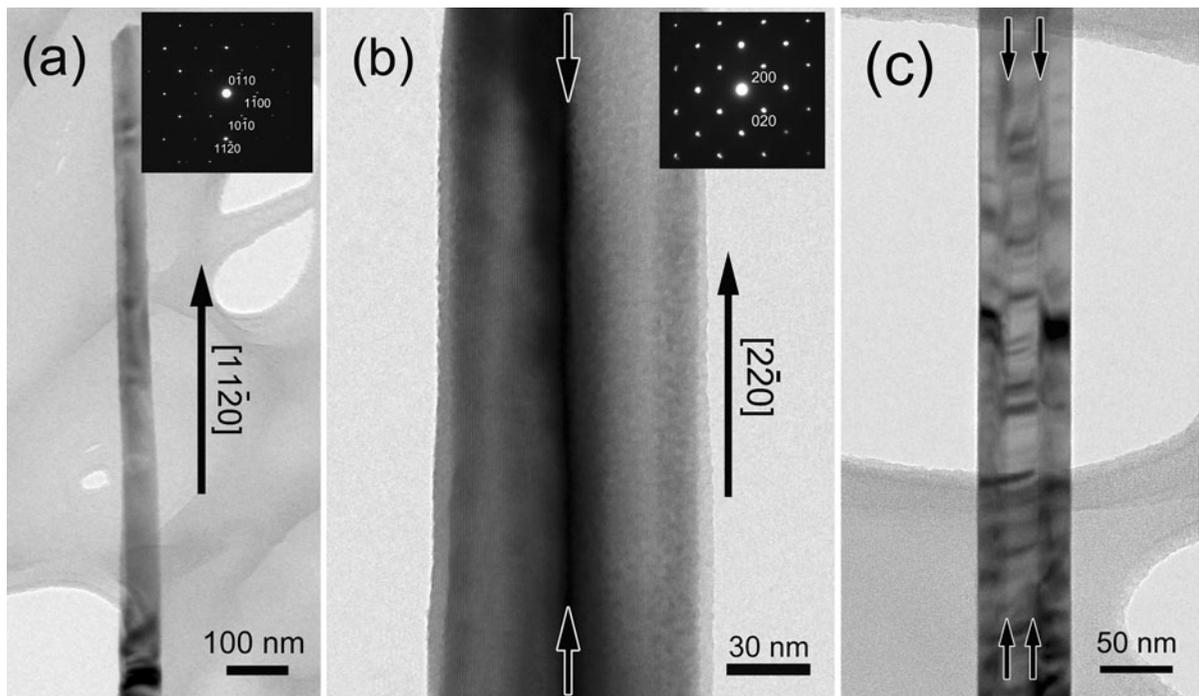
Fig. 2 BF images of three different Fe_2O_3 NWs. **a** Single-crystalline; **b** bicrystalline; and **c** tricrystalline. The *insets* are the corresponding SAED patterns

experienced a structural modulation. Two features should be noted from the TEM observations. First, Fe_2O_3 layer is composed of many grains, and their crystal structures are not the same. Two different structures have been observed for the grains in the Fe_2O_3 layer: hexagonal α-Fe_2O_3 and cubic γ-Fe_2O_3. No ε-Fe_2O_3 grains have been observed, which may result from the instability of ε-Fe_2O_3 at 600 °C. Second, on the surface of Fe_2O_3 layer, two kinds of Fe_2O_3 NWs are formed. They have the same crystal structures as the grains in the root regions. The orientations of NWs and their root regions are nearly the same. This suggests that the root regions serve as a structural template for Fe_2O_3 NW nucleation. A typical BF TEM image with grain A tilted to a zone-axis is shown in Fig. 1c. It can be seen from Fig. 1c that Fe_2O_3 layer is indeed composed of many grains, and the boundaries between the grains are clear.

Further TEM and HRTEM examinations have also been carried out to investigate the microstructures of Fe_2O_3 NWs. Based on the observations of over 100 NWs, three different kinds of morphologies have been found: single-crystalline, bicrystalline, and tricrystalline NWs, as shown in Fig. 2. The surfaces of these

different NWs are smooth. The insets in Fig. 2a and b are the SAED patterns corresponding to the single-crystalline and bicrystalline NWs, respectively. The growth directions for single-crystalline and bicrystalline Fe_2O_3 NWs are indicated by black arrows, which are determined from the SAED patterns. It can be clearly seen from Fig. 2b and c that the interfaces of bicrystalline and tricrystalline NWs are along their length directions, as marked by arrows. From the analysis of the SAED pattern in Fig. 2b, only one set of diffraction dots can be found in the SAED pattern, and the interface between the left and right part of the bicrystalline NW is coherent. The detailed microstructure of single-crystalline NWs and the crystal orientation relationship in between bicrystalline and tricrystalline NWs will be discussed in the following sections.

The differences in the electronic structures of the three different Fe_2O_3 NWs are investigated by EELS. Figure 3a–c are the EELS spectra acquired from an individual single-crystalline, bicrystalline, and tricrystalline NWs, respectively. The insets show the magnified features of O–K edges for the three Fe_2O_3 NWs, respectively. Two peaks, O–K edge ($\sim$532 eV) and
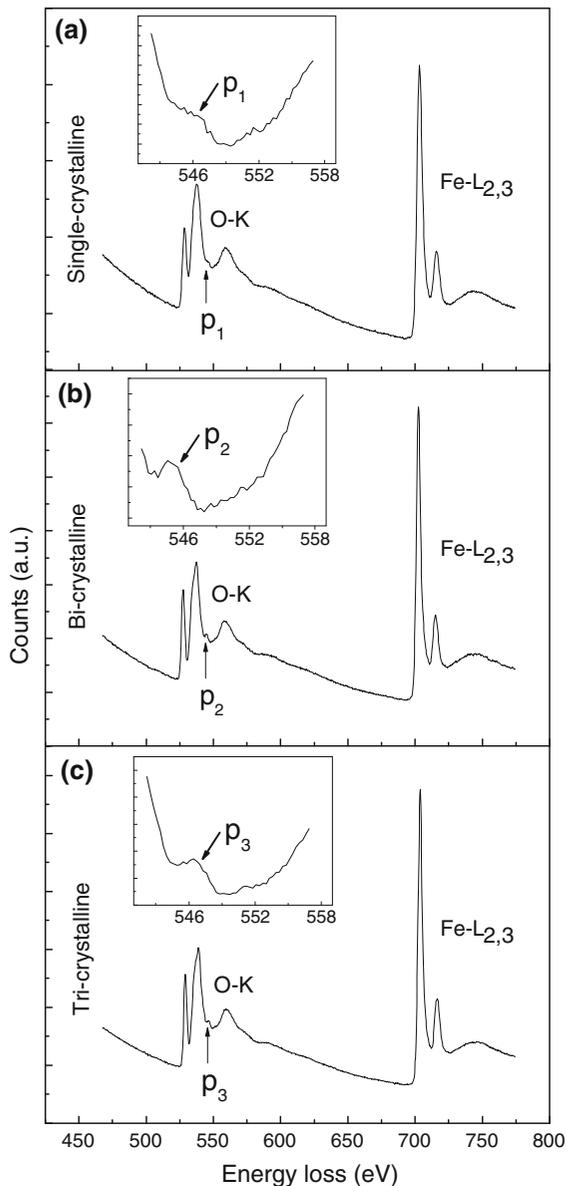
Fig. 3 EELS spectra of **a** a single-crystalline NW; **b** a bicrystalline NW; and **c** a tricrystalline NW. The *insets* are magnified features of the O–K edges

Fe–$L_{2,3}$ edge ($\sim$703 eV), can be easily seen from Fig. 3. Colliex et al. (1991) found that bulk Fe_2O_3 with different crystal structures had different fine structures for O–K edges, reflecting that they have different electronic structures. They reported that a small peak can be seen at about 545–550 eV for γ-Fe_2O_3, but not for α-Fe_2O_3. In our EELS spectra between 545 and 550 eV, P_2 ($\sim$545.5 eV) and P_3 ($\sim$546.3 eV) can be

clearly seen in the insets of Fig. 3b and c, respectively. However, the peak at 545–550 eV is not very evident in Fig. 3a, which is consistent with the results obtained by Colliex et al. (1991). This further confirms that the bicrystalline and the tricrystalline NWs are both composed of γ-Fe_2O_3, but the single-crystalline NWs belong to α-Fe_2O_3. In addition, they have definitely different electronic structures due to the evident differences in crystal structure and bonding environments. It should be noted that there is a chemical shift of 0.8 eV in O–K edge positions for the bicrystalline and tricrystalline NWs, which may arise from different lattice arrangements.

Figure 4a is a representative BF TEM image of a single-crystalline NW with a diameter of about 50 nm and a length of about 1.1 μm. Figure 4b shows the SAED pattern taken from the individual NW in Fig. 4a, which corresponds to a [0001] zone-axis of hexagonal α-Fe_2O_3. To show the hexagonal symmetry of [0001] zone-axis more clearly, six diffraction spots are indicated by circles. The growth direction is determined to be [11$\bar{2}$0]. In the SAED pattern, the superlattice diffraction spots indicated by arrows are caused by a structural modulation. This can be clearly seen from the HRTEM image in Fig. 4c. In Fig. 4c, (3$\bar{3}$00) lattice planes are marked by two parallel white lines. The modulated stripes, which are parallel to the longitudinal axis direction, exist in HRTEM image of single-crystalline Fe_2O_3 NW. To further clarify the nature of the structural modulation, an enlarged HRTEM image is shown in Fig. 4d. It can be seen that the atomic sequences are disturbed at the locations of stripes. The lattice planes of (11$\bar{2}$0) have a shift of 1/2 interplanar spacing, which is a characteristic of a stacking fault. The shift has been indicated by two parallel white lines in Fig. 4d. Accompanying with the periodical shift of the lattice planes, modulated structures are produced. Hence, the well-established fact is that the modulated structure is caused by periodical appearance of stacking faults in the single-crystalline NWs. The periodicity of modulated structure is about 1.53 nm, which is ten times of (3$\bar{3}$00) interplanar spacing. This suggests that the modulated structure consists of ten crystal planes, with every ten crystal planes producing a stacking fault, which has been marked out in the Fig. 4d. Chen et al. (2008b), Cvelbar et al. (2008) and Lee et al. (2007) have reported a modulated structure in the Fe_2O_3 NWs, and
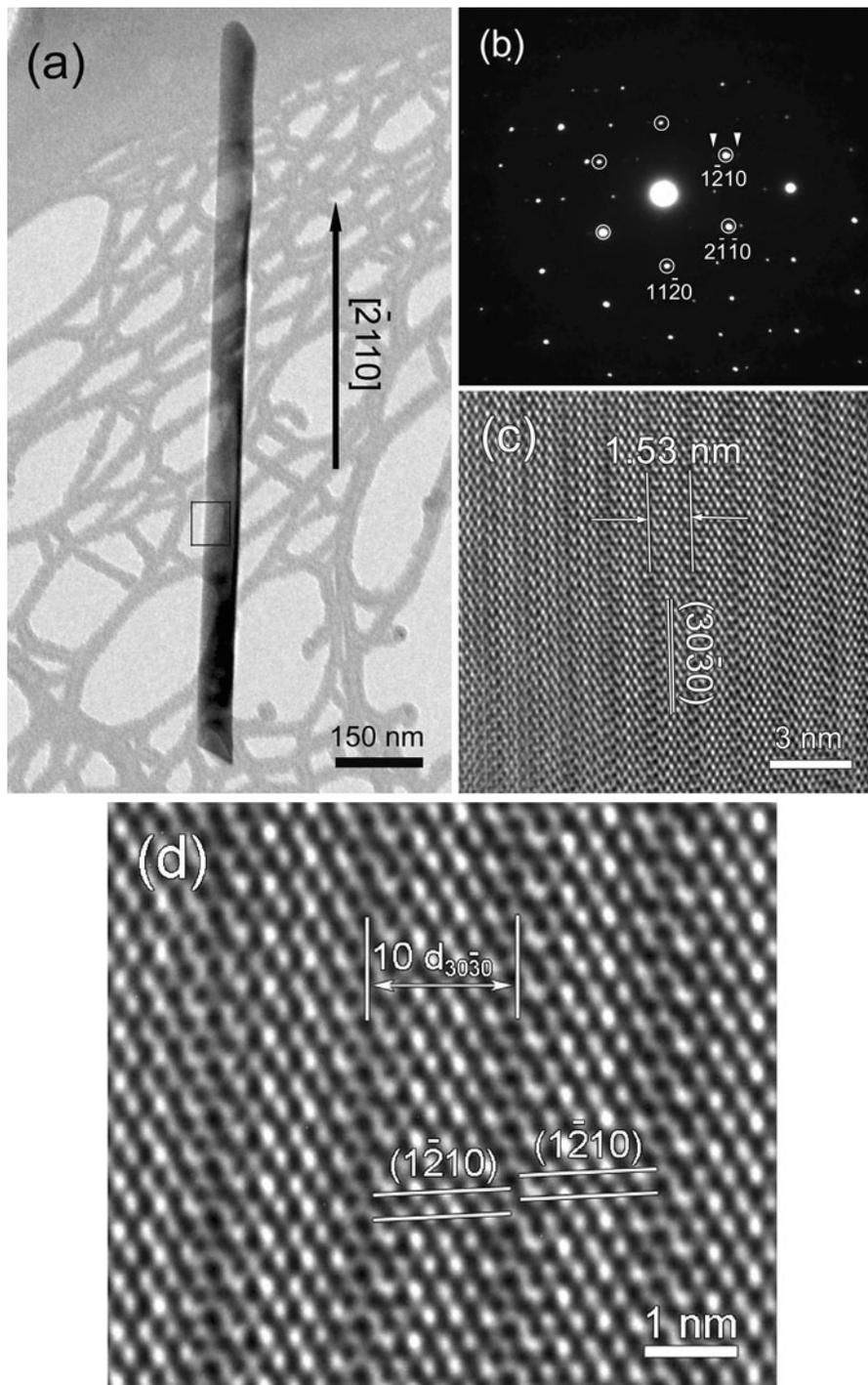
Fig. 4 **a** BF TEM image of single-crystalline Fe_2O_3 NW; **b**, **c** SAED pattern and HRTEM image corresponding to the NW in (**a**); and **d** magnified HRTEM image of (**c**)

they believed that the long-range ordering of oxygen vacancies produced the modulated structure. In our previous study, the stacking faults in Si nanocrystals have been well studied using HRTEM (Wang et al. 2005b). The Si vacancies gathering together on {111} planes could produce intrinsic stacking faults. This is

because {111} planes have the lowest energy in Si nanocrystals. Here, for the single-crystalline Fe_2O_3 NWs, we believe that the existence of shear stress along ($3\bar{3}00$) planes results in the periodical appearance of stacking faults, which eventually produces the modulated structure. It should be noted that in some literature, a similar diffraction pattern (Fig. 4b) has also been indexed as the bicrystalline structure (Voss et al. 1982). However, according to our calculations, the indexing as a modulated structure is more reasonable. The reasons are as follows. First, in our HRTEM image (Fig. 4c), the lattice stripes are very obvious, and their periodicity matches well with the spacing calculated from the superlattice diffraction dots. Second, the smaller diffraction dots in Fig. 4b cannot be completely indexed if the SAED pattern is indexed as the bicrystalline structure. However, if the diffraction pattern is indexed as single-crystalline modulated structure, all the smaller diffraction dots can be correctly indexed.

Based on our observations and previous study (Chen et al. 2008b; Jiang et al. 2003; Kumar et al. 2004), the formation process of the modulated structure in the single-crystalline NW is schematically demonstrated in Fig. 5. During the oxidation process of Fe foils, the three-layered structure is initially formed on the surface of the iron foil. Since the specific volume of Fe_2O_3 is slightly larger than that of Fe_3O_4, compressive stresses are generated and accumulated at the interface between Fe_3O_4 and Fe_2O_3 because of the volume shrinkage. Under the influence

of the compressive stress, the three oxide layers which are composed of many grains will get thicker and thicker. Through the outward diffusion of Fe ions along the grain boundaries, iron cations are deposited onto the Fe_2O_3 grains, where Fe_2O_3 grains serve as the structural templates for Fe_2O_3 NW nucleation. During the growth process, shear stress could be produced inside the Fe_2O_3 NWs. With the increase of time, Fe_2O_3 NWs become longer, and the shear stress becomes larger. When the shear stress accumulates to some extent, stacking faults will form in the Fe_2O_3 NWs. Eventually, the modulated structures accompany with the formation of stacking faults in the single-crystalline NWs.

Figure 6a is a representative BF image of the bicrystalline Fe_2O_3 NW with a diameter of about 25 nm. Figure 6b and c are the corresponding HRTEM image and SAED pattern for the Fe_2O_3 NW in Fig. 6a, respectively. The (200) and (020) lattice planes are marked out by two pairs of parallel white lines. From the analysis of SAED pattern and HRTEM image, three points can be deduced. First, the growth direction of NW is determined to be [$2\bar{2}0$], and the bicrystalline NW is composed of two cubic γ-Fe_2O_3 NWs forming a twinning structure. This is clearly different from the single-crystalline NWs. Second, no appearance of modulated stripes can be found in the HRTEM image, which suggests that the cubic NWs do not experience any structural modulation. Also, this point can be confirmed by the SAED pattern, in which no superlattice spots can be found. Finally, in the

Fig. 5 Schematic illustration of the formation process for the modulated structure in single-crystalline NWs
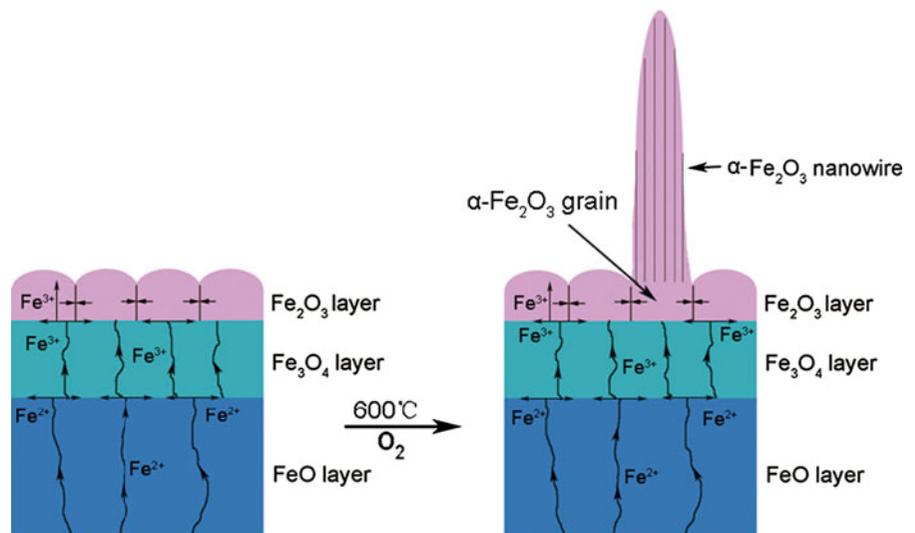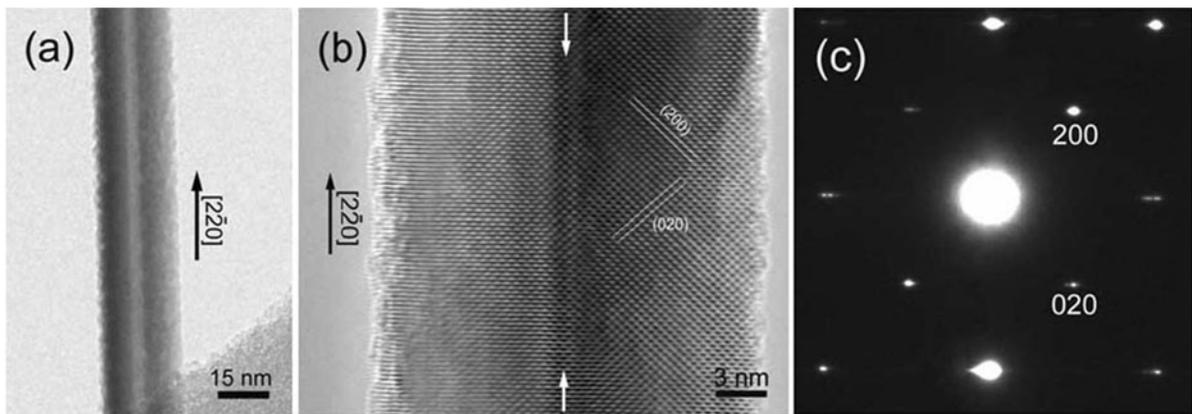
Fig. 6 **a** BF image of bicrystalline Fe_2O_3 NW; **b** and **c** HRTEM image and SAED pattern corresponding to the NW in (**a**)

bicrystalline NW, the interface is parallel to its growth direction, and no stacking faults or dislocations exist in the NW which suggests that the lattice planes in the two wires match well. This confirms that a bicrystalline wire results from the coalescence of two single wires with a cubic structure during the growth process. It should be noted that not all the bicrystalline NWs have the same growth direction because the coalescence could happen for two single-crystalline NWs with different orientations.

Figure 7a–c are typical HRTEM images corresponding to the left, middle, and right parts of the tricrystalline NW in Fig. 2c, respectively. The interfaces between every two parts are very clear, both parallel to its growth direction. The dimension of the left part is about 13 nm, whereas the right part is about 16 nm. The interplanar spacing of the lattice planes marked by two parallel white lines is 3.42 Å, matching well with the calculated spacing of $(\bar{1}2\bar{1})$ planes in cubic γ-Fe_2O_3 ($a = 8.34$ Å). Figure 7d shows the Fourier transform of the HRTEM image in Fig. 7c, from which the growth direction for the right part of the tricrystalline NW is determined to be $[52\bar{1}]$. Based on the analysis of the lattice image in Fig. 7c and the Fourier transform pattern in Fig. 7d, it is confirmed that the tricrystalline NWs belong to cubic γ-Fe_2O_3. No modulated structure exists in the tricrystalline NWs. The tricrystalline wire can also be regarded as a coalescence result of three single-crystalline wires with cubic structures during the growth process. Because coalescence could occur for three NWs with different orientations, the growth directions of three parts are not the same.

Our previous study showed that coalescence could take place in other cubic nanomaterials such as Si nanocrystals (Wang et al. 2005c) and Au nanoparticles Wang et al. (2009). For the Au and Si nanoparticles, two or more smaller particles can combine into a bigger one through the {111} facets. For the cubic γ-Fe_2O_3 NWs, the coalescence behavior is completely different. For the bicrystalline NWs, two single-crystalline NWs combine into one through the {220} planes, while for the tricrystalline NWs, the coalescence takes place through the {211} planes. For those with a hexagonal structure, the coalescence of smaller nanoparticles or NWs has not been observed yet, which is consistent with our results. Herein, the growth mechanism of the bicrystalline and tricrystalline NWs can be explained by the coalescence of two or three single-crystalline NWs. Figure 8 is a schematic diagram for the formation of the bicrystalline NWs. During the formation of the Fe_2O_3 NWs, single-crystalline NWs with cubic and hexagonal structures coexist. With the increase of processing time, the NWs get denser and denser. Owing to volume effect, the adjacent two single-crystalline NWs with a structure of cubic γ-Fe_2O_3 could coalesce into one at a relatively high temperature. Hence, the bicrystalline NWs with a structure of cubic γ-Fe_2O_3 are formed on the surface of the substrate. Similarly, the tricrystalline NWs are formed by the coalescence of three single-crystalline cubic NWs. The reasons for the dominance of single-crystalline NWs are as follows. First, the hexagonal α-Fe_2O_3 is more stable than cubic γ-Fe_2O_3 at 600 °C, and single-crystalline NWs with a hexagonal structure are much more than those with a cubic structure.
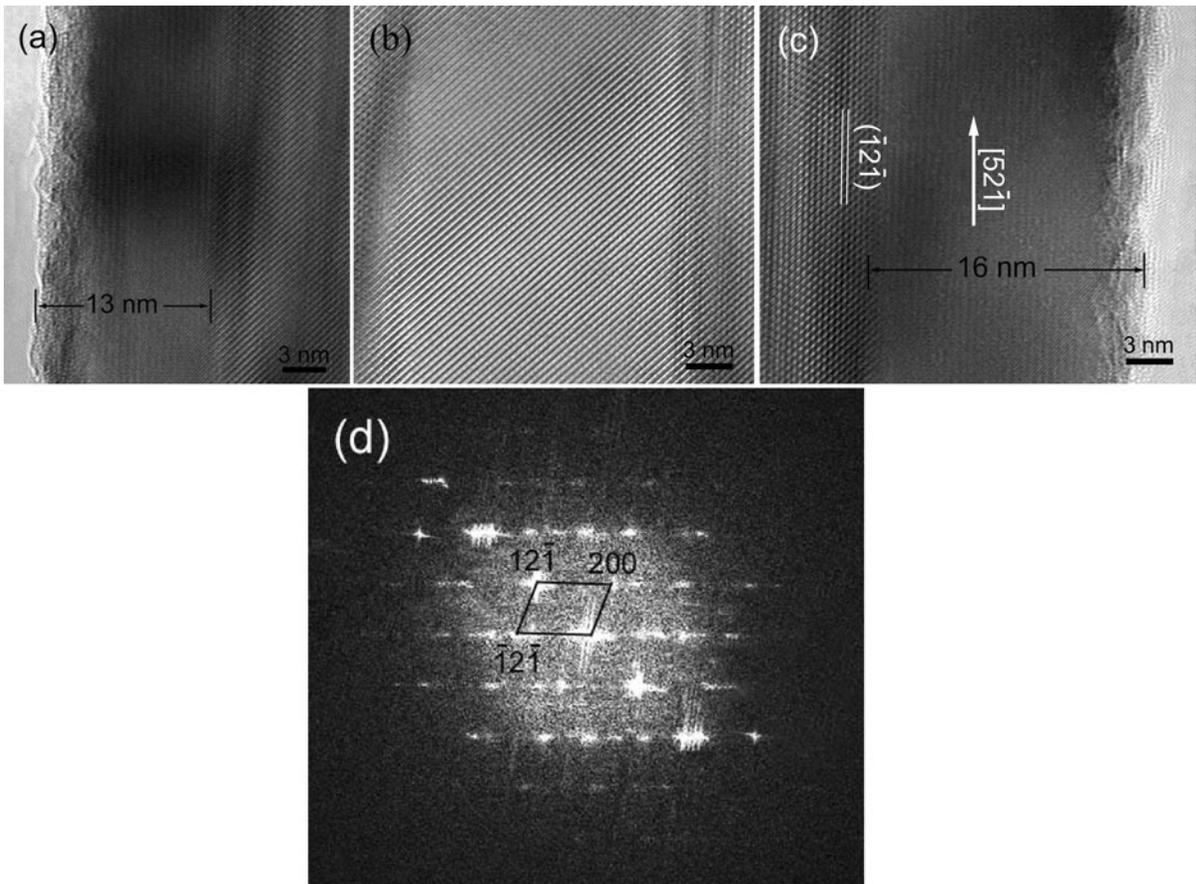
Fig. 7 HRTEM images of tricrystalline Fe_2O_3 NW. **a** The *left*; **b** the *middle*; **c** the *right* part of the tricrystalline NW; and **d** Fourier transform of (**c**)
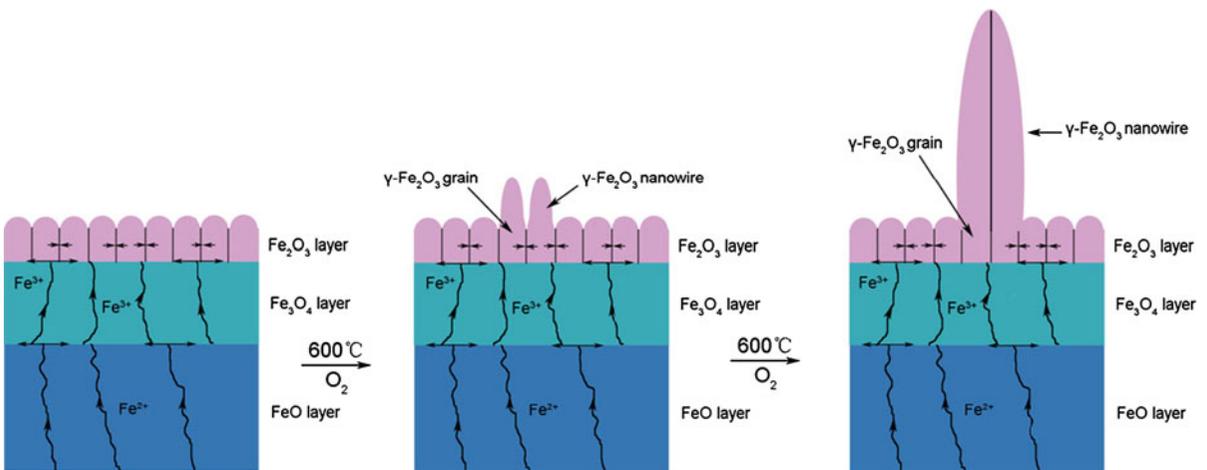
Fig. 8 Schematic diagram for the formation process of the bicrystalline NWs in an oxygen atmosphere

Second, the temperature is not uniform for the entire foil, and it might be lower than 600 °C in some regions. During the oxidation of Fe, more hexagonal α-Fe_2O_3 grains are formed which can serve as more growth templates for Fe_2O_3 NWs, and then more hexagonal α-Fe_2O_3 single-crystalline NWs are formed on the surface of the α-Fe_2O_3 grains.

From the observations of the three different kinds of NWs, a very interesting phenomenon is that the modulated structure only exists in the single-crystalline NW which has the structure of hexagonal α-Fe_2O_3, but not in bicrystalline and tricrystalline NWs with a cubic structure. Based on the above results, a reasonable explanation can be deduced. The NWs with the cubic γ-Fe_2O_3 structure are easier to coalesce into bicrystalline or tricrystalline, whereas those with the hexagonal α-Fe_2O_3 are not. The bicrystalline and tricrystalline NWs are formed by the coalescence of two or three single-crystalline NWs, and no staking faults will form. Hence, the modulated structure only exists in the single-crystalline NWs, but not in the bicrystalline and tricrystalline NWs.

Conclusions

In conclusion, three different kinds of Fe_2O_3 NWs were synthesized by thermal oxidation of Fe foils: single-crystalline, bicrystalline, and tricrystalline. The modulated structure is observed only in the single-crystalline NWs, but not in the others. The formation of the modulated structure is attributed to the periodical appearance of stacking faults in the single-crystalline NWs, which are caused by an accumulation of shear stress in the NWs. The bicrystalline and tricrystalline NWs are formed by the coalescence of two or three single-crystalline NWs, and no stacking faults will form. This is the reason why the modulated structure only exists in the single-crystalline NWs, but not in the bicrystalline and tricrystalline NWs.

References

Bjork MT, Ohlsson BJ, Sass T, Persson AI, Thelander C, Magnusson MH, Deppert K, Wallenberg LR, Samuelson L (2002) One-dimensional steeplechase for electrons realized. Nano Lett 2:87–89

Chen J, Xu L, Li W, Gou X (2005) α-Fe_2O_3 nanotubes in gas sensor and lithium-ion battery applications. Adv Mater 17:582–586

Chen JT, Zhang F, Wang J, Zhang GA, Miao BB, Fan DY, Yan PX (2008a) CuO nanowires synthesized by thermal oxidation route. J Alloys Compd 454:268–273

Chen ZQ, Cvelbar U, Mozetic M, He JQ, Sunkara MK (2008b) Long-range ordering of oxygen-vacancy planes in α-Fe_2O_3 nanowires and nanobelts. Chem Mater 20:3224–3228

Chueh YL, Lai MW, Liang JQ, Chou LJ, Wang ZL (2006) Systematic study of the growth of aligned arrays of α-Fe_2O_3 and Fe_3O_4 nanowires by a vapor–solid process. Adv Funct Mater 16:2243–2251

Colliex C, Manoubi T, Ortiz C (1991) Electron-energy-loss-spectroscopy near-edge fine structures in the iron-oxygen system. Phys Rev B 44:11402–11411

Cornell RM, Schwertmann U (2003) The iron oxides: structure, properties, reactions, occurrences and uses. Wiley, New York

Cvelbar U, Chen ZQ, Sunkara MK, Mozetic M (2008) Spontaneous growth of superstructure α-Fe_2O_3 nanowire and nanobelt arrays in reactive oxygen plasma. Small 4: 1610–1614

Dong Z, Kashkarov P, Zhang H (2010) Monte Carlo study for the growth of α-Fe_2O_3 nanowires synthesized by thermal oxidation of iron. Nanoscale 2:524–528

Fu YY, Chen J, Zhang H (2001) Synthesis of Fe_2O_3 nanowires by oxidation of iron. Chem Phys Lett 350:491

Goncalves AM, Campos LC, Ferlauto AS, Lacerda RG (2009) On the growth and electrical characterization of CuO nanowires by thermal oxidation. J Appl Phys 106:034303

Gudiksen MS, Lauhon LJ, Wang JF, Smith DC, Lieber CM (2002) Growth of nanowire superlattice structures for nanoscale photonics and electronics. Nature 415:617–620

Han Q, Liu ZH, Xu YY, Chen ZY, Wang TM, Zhang H (2007) Growth and properties of single-crystalline γ-Fe_2O_3 nanowires. J Phys Chem C 111:5034–5038

Hiralal P, Unalan HE, Wijiayantha KGU, Kursumovie A, Jefferson D, MacManus-Driscoll JL, Amaratunga GAJ (2008) Growth and process conditions of aligned and patternable films of iron(III) oxide nanowires by thermal oxidation of iron. Nanotechnology 19:455608

Jiang Y, Meng XM, Liu J, Hong ZR, Lee CS, Lee ST (2003) ZnS nanowires with wurtzite polytype modulated structure. Adv Mater 15:1195–1198

Kumar A, Srivastava AK, Tiwari P, Nandedkar RV (2004) The effect of growth parameters on the aspect ratio and number density of CuO nanorods. J Phys Condens Matter 16: 8531–8543

Lee YC, Chueh YL, Hsieh CH, Chang MT, Chou LJ, Wang ZL, Lan YW, Chen CD, Kurata H, Isoda S (2007) p-type α-Fe$_2$O$_3$ nanowires and their n-type transition in a reductive ambient. Small 3:1356–1361

Liu SQ, Huang KL (2005) Straightforward fabrication of highly ordered TiO$_2$ nanowire arrays in AAM on aluminum substrate. Sol Energy Mater Sol Cells 85:125–131

Mema R, Yuan L, Du QT, Wang YQ, Zhou GW (2011) Effect of surface stresses on CuO nanowire growth in the thermal oxidation of copper. Chem Phys Lett 512:87–91

Nasibulin AG, Rackauskas S, Jiang H, Tian Y, Mudimela PR, Shandakov SD, Nasibulina LI, Sainio J, Kauppinen EI (2009) Simple and rapid synthesis of α-Fe$_2$O$_3$ nanowires under ambient conditions. Nano Res 2:373–379

Rachauskas S, Nasibulin AG, Jiang H, Tian Y, Kleshch VI, Sainio J, Obraztsova ED, Bokova SN, Obraztsov AN, Kauppinen EI (2009) A novel method for metal oxide nanowire synthesis. Nanotechnology 20:165603

Shimojo M, Takeguchi M, Furuya K (2006) Formation of crystalline iron oxide nanostructures by electron beam-induced deposition at room temperature. Nanotechnology 17:3637

Srivastava H, Tiwari P, Srivastava AK, Nandedkar RV (2007) Growth and characterization of α-Fe$_2$O$_3$ nanowires. J Appl Phys 102:054303

Tepper T, Ilievski F, Ross CA, Zaman TR, Ram RJ, Yung SY, Stadler B (2003) Magneto-optical properties of iron oxide films. J Appl Phys 93:6948–6950

Voss DA, Butler EP, Mitchell TE (1982) The growth of hematite blades during the high temperature oxidation of iron. Metall Mater Trans A 13:929–935

Wang RM, Chen YF, Fu YY, Zhang H, Kisielowski C (2005a) Bicrystalline hematite nanowires. J Phys Chem B 109: 12245–12249

Wang YQ, Smirani R, Ross GG (2005b) Stacking faults in Si nanocrystals. Appl Phys Lett 86:221920

Wang YQ, Smirani R, Ross GG, Schiettekatte F (2005c) Ordered coalescence of Si nanocrystals in SiO$_2$. Phys Rev B 71:161310R

Wang YQ, Liang WS, Geng CY (2009) Coalescence behavior of gold nanoparticles. Nanoscale Res Lett 4:684–688

Wen XG, Wang SH, Ding Y, Wang ZL, Yang SH (2005) Controlled growth of large-area, uniform, vertically aligned arrays of α-Fe$_2$O$_3$ nanobelts and nanowires. J Phys Chem B 109:215

Yuan L, Wang YQ, Mema R, Zhou GW (2011) Driving force and growth mechanism for spontaneous oxide nanowire formation during the thermal oxidation of metals. Acta Mater 59:2491–2500

Yuan L, Wang YQ, Cai RS, Jiang QK, Wang JB, Li BQ, Sharma A, Zhou GW (2012) The origin of hematite nanowire growth during the thermal oxidation of iron. Mater Sci Eng B 177:327–336

Zhang DH, Liu ZQ, Hau S, Li C, Lei B, Stewart MD, Tour JM, Zhou CW (2004) Magnetite (Fe$_3$O$_4$) core-shell nanowires: synthesis and magnetoresistance. Nano Lett 4:2151–2155